

Contents lists available at ScienceDirect

Petroleum Science

journal homepage: www.keaipublishing.com/en/journals/petroleum-science



Original Paper

Regulating carbonaceous mesophase structure by controlling nitrogen-containing aromatics of FCC slurry oil: Insights from MD simulations and experimental studies



Xing-Guo Wei ¹, Yuan-Qin Zhang ¹, Ling-Rui Cui, Cao Liu, Jian Huang, Fa-Hai Cao ¹

School of Chemical Engineering, East China University of Science and Technology, Shanghai, 200237, China

ARTICLE INFO

Article history:
Received 16 November 2024
Received in revised form
20 February 2025
Accepted 23 March 2025
Available online 28 March 2025

Edited by Min Li

Keywords:
MD with ReaxFF
Pyrolysis behavior
Mesocarbon microbeads
Application of heavy oil
Nitrogen-containing aromatics
Morphology and structure

ABSTRACT

The influence of nitrogen-containing polycyclic aromatic hydrocarbons (NC-PAH) on the formation of carbonaceous mesophase remains enigmatic, despite extensive research on the production of carbonaceous materials from aromatic-rich oils. Molecular dynamics simulation was used to investigate the variations in pyrolysis behavior between PAH and NC-PAH based on the composition analysis. Through adjusting the content of NC-PAH, the influence of NC-PAH on the thermal stability of slurry oils (SOs) was evaluated by thermogravimetry, viscosity, coke value, and quinoline insoluble (OI). The morphology and structure of mesocarbon microbeads (MCMBs) prepared with SOs were measured by a polarized-light microscope, SEM, XRD, and Raman. Simulation results indicate that NC-PAH possesses much higher reactivity and tends to produce highly condensed solid and coke products. It corresponds to the QI and high viscosity in thermal stability experiments. Therefore, high concentrations of NC-PAH result in nonuniform morphology and disordered structures. In a system with low viscosity and few QIs, SO, which has a low nitrogen content (475 ppm), reacts gently to produce MCMBs with a uniform particle size (10-40 μm) and an excellent spherical shape. As NC-PAH content decreases, the crystalline size of graphitization elevates, as evidenced by parallel layers (10.472-11.764) and stack height (3.269 -3.701 nm). The graphitization degree becomes worse and nonuniform with the increase of the content of NC-PAH, and the best is 20.58% evaluated by Raman spectra area ratio (A_G/A_{all}) . Overall, this work suggests a nitrogen content reference and a controlling technology of nitrogen for the preparation of superior MCMB.

© 2025 The Authors. Publishing services by Elsevier B.V. on behalf of KeAi Communications Co. Ltd. This is an open access article under the CC BY-NC-ND license (http://creativecommons.org/licenses/by-nc-nd/4.0/).

1. Introduction

Aromatic-rich oils (ARO) such as fluid catalytic cracking slurry oil (SO) and coal tar oil are yield-rich by-products of petroleum refining process and coal chemical process. These AROs possess low combustion properties and refining values due to heavy compositions and heteroatoms (Kim et al., 2012; Li et al., 2016; Song et al., 2018; Guo et al., 2020a). The high value-added application of AROs should be given more attention due to the urgent demand for light fuels and the ever-increasing inferior and heavier nature of crude oil (Guo et al., 2020b). The synthesis of mesocarbon microbeads

(MCMB) from aromatic-rich oils presents a compelling avenue for its production, boasting benefits of environmental friendliness, and economic efficiency (Li et al., 2005; Guo et al., 2020b; Gong et al., 2021, 2022). The potential applications of MCMB covers Li-ion battery anode, column separators, and high-surface active carbon (Wang et al., 1999a, 1999b; Haratake et al., 2007; Zhong et al., 2020).

Coal tar pitch is broadly used as the feedstock of MCMB, while the preparation of MCMB from SO has rarely been studied (Li et al., 2005; Yang et al., 2011; Guo et al., 2020b). Yang et al. (2011) suggested that avoiding the formation of bulk products is significant to obtain MCMB with high quality. However, asphaltenes (Li et al., 2018; Yu et al., 2019; Guo et al., 2020a; Jiao et al., 2021), olefins (Jiao et al., 2020), and heterocyclic aromatics (HA) (Oi et al., 1978; Mochida et al., 1991; Jin et al., 2011; Sun et al., 2022) in SO possess higher reactivity, so that these undesirable components not only possibly generate negative influences on the shape and particle size distribution of MCMB but also possibly tend to lead to chaotic

E-mail address: fhcao@ecust.edu.cn (F.-H. Cao).

Peer review under the responsibility of China University of Petroleum (Beijing).

¹ These authors contributed equally.

^{*} Corresponding author.

isotropic structures. Consequently, prior to heat treatment, some pretreatment is required to adjust the composition. Several methods for adjusting the composition of ARO were reported. With the processes of hydrotreatment, distillation, extraction, and oil mixing, the macro group composition was altered (Li et al., 2018; Zhang et al., 2018; Yu et al., 2019; Guo et al., 2020a; Jiao et al., 2020, 2021). Then, the influences of aromaticity, asphaltenes, and solvent-insoluble substances on the morphology and inner structures of carbonaceous mesophase were researched. Furthermore, it appears that the pyrolysis behaviors are influenced by the type and quantity of trace heterocyclic polycyclic aromatic hydrocarbons (PAHs) (Sanada et al., 1973; Mochida et al., 1991; Ayyappan and Choudhary, 2016; Sun et al., 2022), which gets less attention. As the great feedstock oil of carbonaceous materials, the sulfur content should be low to 0.7 wt% (Jin et al., 2011). It can be easily realized by hydrodesulfurization (Mochida et al., 1988; Ayyappan and Choudhary, 2016; Guo et al., 2020a; Jiao et al., 2021). However, nitrogen-containing PAH (NC-PAH) possesses a stronger C-N bond, so the efficiency of hydro-denitrification is much lower than hydrodesulfurization under the same conditions (Ayyappan and Choudhary, 2016; Vázquez-Garrido et al., 2019; Guo et al., 2021; Yin et al., 2021; Liu et al., 2022). Aromatic rings of PAH will be saturated due to over hydrogenation under intense hydrotreatment conditions (Ayyappan and Choudhary, 2016; Guo et al., 2021; Liu et al., 2021; Yin et al., 2021). Nitrogen removal is also difficult to realize physically because of the similar conjugate structures of PAH and NC-PAH (Yan et al., 2020; Zhao et al., 2022). There is no appropriate nitrogen regulation technology for ARO, and the influences of nitrogen on pyrolysis behaviors are ambiguous. Furthermore, systematic experimental investigations remain scarce regarding the extent to which nitrogen content in SO influences mesophase morphology and graphitization degree. Additionally, whether denitrification pretreatment is necessary to achieve morphologically homogeneous and structurally ordered mesophase development requires further validation. All above is because those experiments are unable to carry out more delicate, even molecular-level adjustments.

Employing molecular dynamics (MD) simulation with a reactive force field (ReaxFF) could provide lots of help in controlling the type and content of PAH and NC-PAH, which is quite difficult in experiments (Zang et al., 2020; Jian et al., 2021; Yang et al., 2021; Jana et al., 2022). Then, the reactive behaviors of different PAH and NC-PAH can be researched. For instance, Jana et al. (2022) explored the mechanical properties of carbon fibers prepared from different pitch molecules under various initial setting system densities with ReaxFF simulation. Jian and co-workers (Jian et al., 2021) revealed the pyrolysis behavior differences of pitch derived from pure aromatics (naphthalene) and oil with ReaxFF. In artificially set systems, the quantity of PAHs can be easily added or subtracted. So, it is convenient to investigate pyrolysis behaviors of various PAH and NC-PAH. It provides a theoretical foundation to regulate the structure of carbonaceous mesophases at the molecular level.

In this work, MD simulation with ReaxFF was first implemented under the characterization data of SO. The pyrolysis behaviors of various types of PAH and NC-PAH were revealed. It was verified that NC-PAH would significantly accelerate the reaction and lead to coking. For regulating the reaction process and properties of MCMB, creative ARO denitrification technology and nitrogen-rich recycled oil blending strategies were developed. MCMBs with uniform morphology and ordered structure could be prepared by using SO after denitrification. The nitrogen content references and regulation methods were suggested for the preparation of high-grade

mesophase carbon materials. This provides the basis and significance for the preparation of advanced mesophase through efficient denitrification.

2. Experiment

2.1. Simulation methods

A set of major PAHs (Fig. S1) with aromatic rings ranging from 2 to 5 were selected as the model PAHs, and alkyl-carbazole (Fig. S1) was selected as the model NC-PAH based on our earlier analysis (Wei et al., 2023) of the PAH composition and NC-PAH form (Table S1). To create a sole-molecule system, 100 molecules were arranged at random into rectangular boxes using Packmol software (Table S2). To find out how NC-PAH affects the pyrolysis behaviors of the SO, different numbers of NC-PAH were inserted into the model SO box, which contains a variety of PAHs according to the PAH composition of the SO. Table S2 contains more information.

The Gaussview established the initial PAH structures (Radovic, 2005). To optimize the geometry of molecules, Gaussian 09 (Frisch et al., 2013) with B3LYP theory and the base set level of TZVP were used (Grimme, 2006). B3LYP and Def2TZVP were used to calculate the atomic charge of the restrained electrostatic potential (RESP) (Schauperl et al., 2020). The wave function analyses such as electrostatic potential, electron density, electron localization function (ELF) and average localized ionization energy (ALIE) were calculated employing Multiwfn (Lu and Chen, 2012). The Generalized Amber Force Field (GAFF) function (Wang et al., 2004) was used by the ANTECHAMBER module (Wang et al., 2006) to generate force field parameters. The software GROMACS (Abraham et al., 2015) was used to carry out the non-reactive equilibration of all systems in the NPT ensemble at 300 K and 1 atm for 50 ns. The particle mesh Ewald (PME) (Darden et al., 1993) was utilized to calculate the long-distance electrostatic interaction, with a 14 Å cutoff distance. A time step of 1 fs was maintained. The temperature and pressure were managed by a Nose-Hoover thermostat (Nosé, 1984; Hoover, 1985) and a Parrinello-Rahman barostat (Taha and Lee, 2013).

The GRO2LAM software package (Chávez Thielemann et al., 2019) transforms the relaxed structure from gro to data format in order to run the reaction molecular dynamics (MD) in LAMMPS (Thompson et al., 2022). At constant volume, all systems were first heated gradually at a rate of 100 K/ps from 300 K to the target thermal treatment temperature. The temperature was then maintained for 300 ps. Considering our simulation capacity (i.e., the reasonable time we can employ for simulation) and experiment time (8 h), the thermal treatment temperature is selected to be 2800 K according to the Arrhenius equation and activation energy (Zang et al., 2020; Jian et al., 2021). A timestep of 0.2 fs was used for all simulations. It was the reactive potential from the work of van Duin et al. (Castro-Marcano et al., 2012; Jian et al., 2019) that we used to explain interatomic interactions. A Nose-Hoover thermostat (Nosé, 1984; Hoover, 1985) was used to control the temperature of all simulations, and the damping parameter was selected to be 100 timesteps. To recognize various species, the bond order cutoff was set at 0.3. OVITO (Stukowski, 2010) was utilized for visualization.

2.2. Synthesis of SO with varying nitrogen concentrations

For getting four various nitrogen content SO, extraction denitrification technology, nitrogen-rich oil recovery method, and blending strategy were created. The SO was obtained from Sinopec Zhenhai Company. The chemical materials used in the experimental extraction process include polyethylene glycol (PEG) and deionized water. The raw oil was named SO. 360 g PEG 2000 (molecular weight is 2000 g/mol) and 120 g water were stirred at 80 °C for at least 60 min to generate a homogeneous liquid. Then, extraction was implemented in a double-layer heat preservation mixing kettle with the weight ratio of 150 g extractant to 150 g SO at 500 rpm, 70 °C, and 30 min. The denitrification SO (DNSO) was collected from the upper phase, and the extraction phase was emitted from the under phase. The extraction was repeated three times to get DNSO. Equally much water was added to the extractive phase. Then, the nitrogen-rich SO was separated from the extraction phase through centrifugation at 6000 rpm for 10 min. 2/3.5 g nitrogen-rich SO and 28/36.5 g SO were combined at 100 °C for 30 min to get SO1 and SO2.

2.3. Thermal stability experiments and preparation of mesophase pitch and MCMB

Four SOs were treated under the same conditions to explore their thermal stabilities and pyrolysis behaviors. About 30 g of SO were placed in a 100 mL vertical tubing bomb reactor. All heat treatments were carried out after three times nitrogen replacement for removing the air. Firstly, the system was heated from room temperature to 350 °C at 7 °C/min and maintained for 60 min with an initial nitrogen pressure of 1 MPa and a stirring rate of 300 rpm. The pressure was controlled by a backpressure valve after the outlet pipe. After that, the reactor was heated to 430 °C at 3 °C/min, and the soaking time was 4 h for thermal stability experiments and 8 h for preparation of mesophase pitch (DNSO-P, SO-P, SO1-P, and SO2-P). Using a Soxhlet extraction device, the thermal condensation pitch was dissolved, filtered, and pyridine insoluble compounds (DNSO-MCMB, SO-MCMB, SO1-MCMB, and SO2-MCMB) were obtained. Then, the MCMB was washed with alcohol and dispersed in alcohol using ultrasound.

2.4. Characterization

Elemental compositions (carbon, hydrogen) of SOs were measured by an elemental analyzer (Elementar Various EL Cube). The nitrogen and sulfur content were determined by an S/N analyzer (JF-TSN-5000) for more precision. The group analysis was carried out according to Chinese Petrochemical Industry Standard (NB/SH/T 0509-2010). The pitches produced after 4 h of heat treatment were examined for various parameters, including viscosity, thermogravimetric curve (TG), coke value (CV), and quinoline insoluble substance (QI), in order to assess the thermal stability of the four SOs. The viscosity was detected by a rotational rheometer (Anton-Paar MAR501) using a pp25 rotor. TG was implemented at Thermo-Gravimetric Analysis (NetzschTGA209F1) under nitrogen atmosphere. The test temperature ranges from 30 to 800 °C, with the temperature increasing rate of 10 °C/min. The CV and QI were measured following GB/T 8727-2008 and GB/T 2293-2019, respectively.

Optical microstructures of pitches were acquired from polarized light optical microscopy (Leica DM4P) after fixing the samples in epoxy and a series of polishing processes. After drying, the morphology analyses of MCMB were investigated by a field-emission scanning electron microscope. The particle size was detected by Laser particle size analyzer (Malvern Mastersizer 3000). X-ray diffraction (XRD, D8 Advance, Cu K α radiation, $\lambda = 0.15418$ nm) analysis was employed to explore the average structure information of MCMB. The Raman spectrum (Thermo

Scientific SXR) was also utilized to analyze the effect of nitrogen on the structural disorder degree and structure uniformity of MCMB.

3. Results and discussion

3.1. Pyrolysis behavior difference between PAHs and NC-PAH

A set of typical PAHs with 2–5 aromatic rings, carbazole type NC-PAH, and dibenzothiophene type sulfur-containing PAH were chosen as the model aromatic molecules (Fig. S1) under the hydrocarbon analysis and nitrogen morphology characterization (Table S1). Sole PAH systems were built (Table S2) to study their thermal radical polycondensation reactive activity. During the thermal treatment at 2800 K, species were recognized by the bonding relationship, which is judged by bond order. The number of initial PAH decreased with the simulation time and transformed into polymers with higher molecular weight. A Python script was used to count these data over time, which was plotted in Fig. 1.

According to our previous characterization of SO (Wei et al., 2023), PAH with fewer aromatic rings has more methyl side chains. These alkyl side chains might be generated from aromatic carbon during large molecules of catalytic cracking feedstock oil were cracked to small PAHs in the catalytic cracking process. So, high content of 2a, 2b, 3a, and 3b with two methyl side chains (Table S2) were selected as the 2-3 aromatic rings model PAH. The 4-5 aromatic rings model PAH chose 4b, 5a, and 5b with few methyl side chains (Table S2). PAHs with five aromatic rings apparently consume slower compared with other PAHs (Fig. 1). The reactive activity order of other PAHs can be ranked as Na \approx Sa > 3a $> 3b > 2a \approx 2b > 4b$ (one methyl side chain). It is demonstrated that the methyl side chain is easier to generate radicals and link PAHs (Trejo et al., 2010). It is heterocyclic PAHs that are focused by this study. Na and Sa notably consume faster than PAHs. Initial Na molecules left over about 15% while other PAHs remain 30%-70% when the simulation time comes to 100 ps. Therefore, NC-PAH and sulfur-containing PAH will lead to a large reaction difference of real ARO and product difference, which will be discussed later in the calculations and experiments.

In addition to consumption rates, the thermal condensation products were divided and investigated. The products were recognized and divided by the following rules: species were recognized by bond order of atom pairs, bond formation judgment threshold, and bond connection relation. Phase state of products

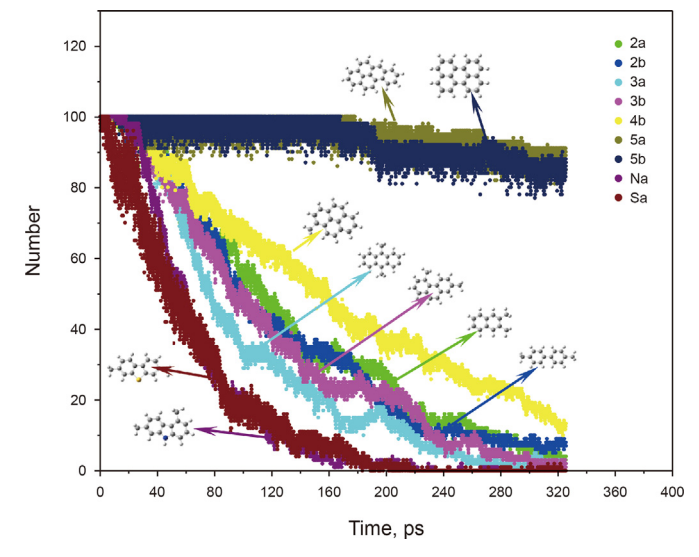


Fig. 1. Molecule consumption rate of various PAHs in sole molecule systems.

was defined by the number of heavy atoms (C, N, S) (Jian et al., 2019, 2021). Molecules containing less than 4 heavy atoms were regarded as gas products (C4). Molecules containing 4-20 heavy atoms (C4-20) were the initial molecules and molecules losing or obtaining radicals. The liquid products (C20-40) had 20-40 heavy atoms. Solid products (C40-100) were defined as species with a number of heavy atoms ranging from 40 to 100. Additionally, species with heavy atoms >100 (C100) were collected to correspond to coke in heat treatment experiments. The weight content of various kinds of products in eight systems containing sole type of molecule were plotted against the simulation time in Fig. 2. In all systems, initial molecules (red lines) reduced along with simulation time. Gas products appeared due to cracking of initial molecules and liquid products generated by radical condensation. It could be observed that gas product yield increased fastest and reached near 10 wt% in the Na system (Fig. 2(h)). It was the Na system in which liquid product yield rose to the highest content (35 wt%) at the earliest time (120 ps) compared with other systems and then descended because liquid products continued to condense to products containing more aromatic rings. It was also the Na system (Fig. 2(h)) that generated the most coke products (60 wt%). The above results demonstrated that NC-PAH tended to produce heavy species, even coke at the early. Subsequently, it will result in high viscosity, which negatively affects the mass and heat transfer and the development of anisotropic mesophase.

3.2. Influence of NC-PAH on pyrolysis behaviors of model SO

In order to explore the effect of nitrogen concentration on the pyrolysis behavior of SO, three models of SO were built. The PAH molecules were placed in boxes according to the hydrocarbon analysis (Table S1). Different numbers of NC-PAHs were inserted into the box to obtain systems a, b, and c. Specific numbers of molecules were listed in Table S2. The nitrogen content of systems a, b, and c is 0, 1774, and 6230 ppm, respectively. The initial molecule consumption rates were presented in Fig. S2. When Na existed, consumption rates of all molecules changed. The 2a PAH totally reacted at 150 ps in systems b and c, while there were some reversible reactions in systems b. 3a, 3b, 4a, 4b, 5a, 5b consumed faster in system b and c than in system a. Though there was less

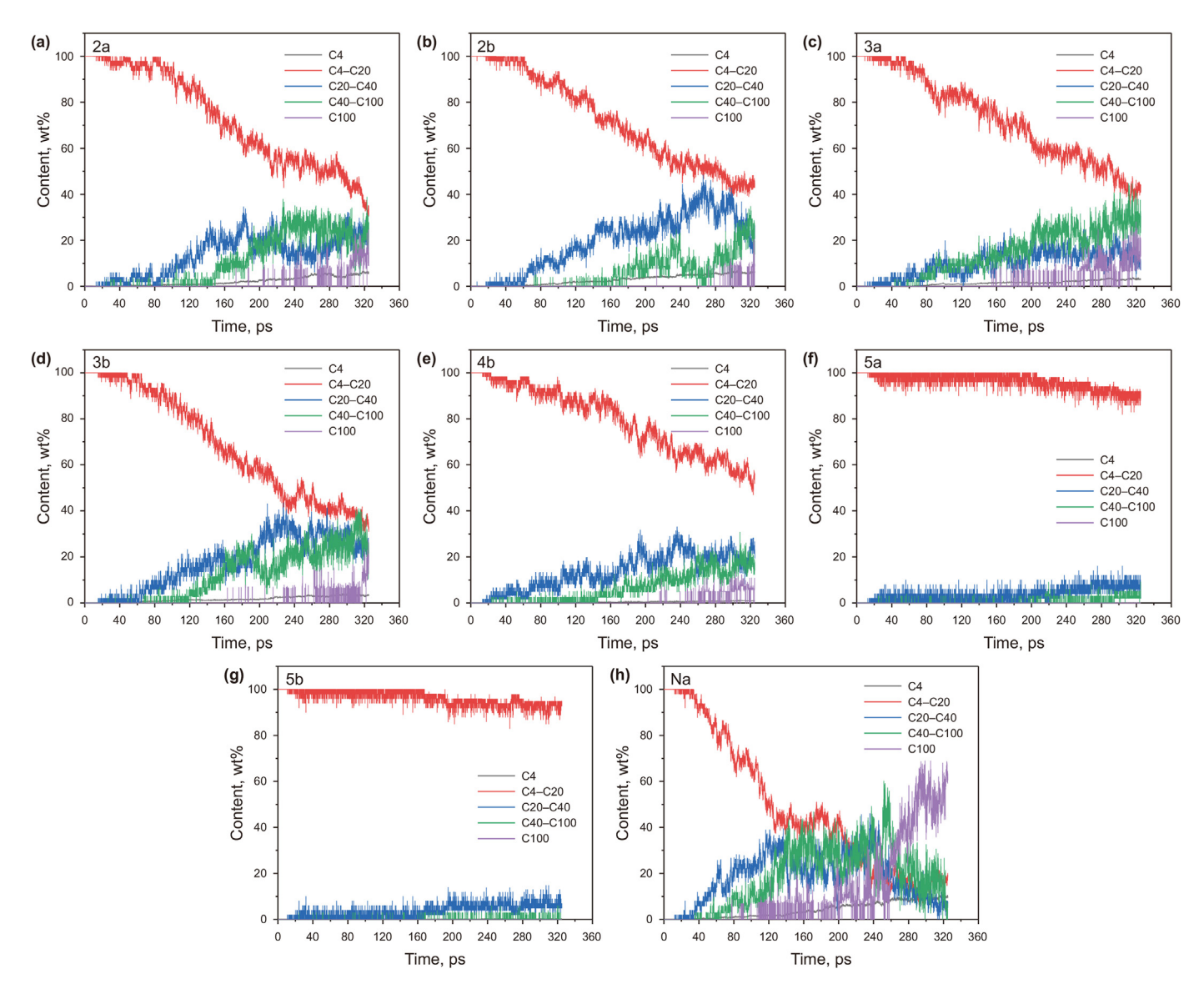


Fig. 2. Product molecules with different numbers of heavy atoms verify with simulation time in sole molecule systems. (a)—(h) are systems 2a, 2b, 3a, 3b, 4b, 5a, 5b, Na. The settings of the sole molecule systems can be found in Table S2. The product molecules containing m heavy atoms are divided into groups Cm.

growth of each type of PAH, total reactive progress was indeed accelerated due to the existence of Na, as shown in Fig. 3(b).

The existence of NC-PAH would also affect the product distribution. As presented in Fig. 3(c), the liquid product yield started to decrease to about 12.5 wt% in system c when the yield reached 20 wt% at near 200 ps. The solid product yield (Fig. 3(d)) rapidly elevated from 5 to 20 wt% during 100-175 ps in system c, then

moderately increased. More coke products containing 100-200 heavy atoms (Fig. 3(e)) were generated in system c (20 wt%) than in systems b and a. No coke products with over 200 heavy atoms were produced in system a, while there was near 7.5 and 5 wt% in systems b and c, respectively (Fig. 3(f)). According to the product transformation phenomenon of systems with varying nitrogen content, it is clear that systems with more nitrogen tend to rapidly

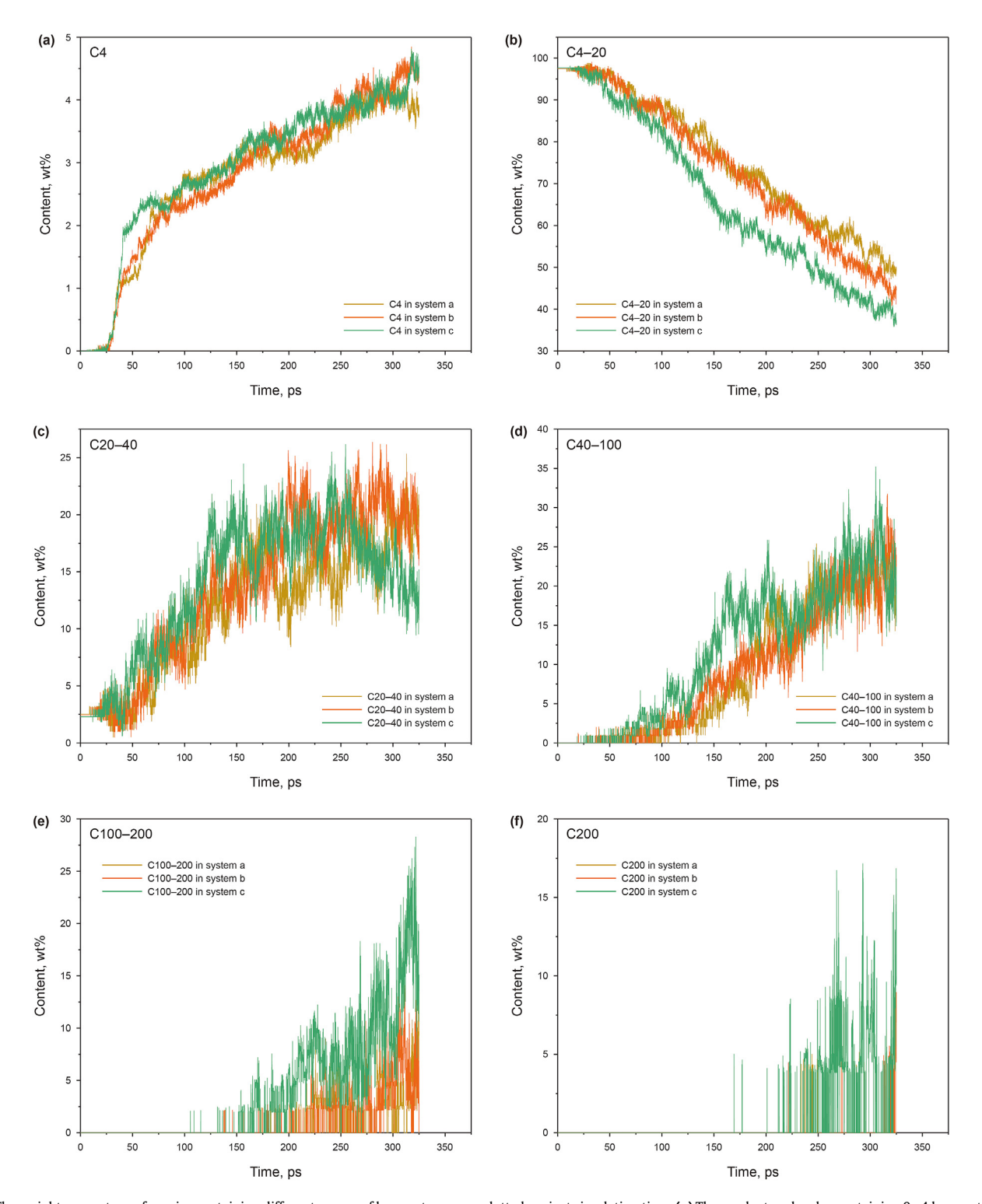


Fig. 3. The weight percentage of species containing different ranges of heavy atoms was plotted against simulation time. **(a)** The product molecules containing 0–4 heavy atoms, **(b)** 4–20, **(c)** 20–40, **(d)** 40–100, **(e)** 100–200, **(f)** >200. The nitrogen content of systems a, b, and c is 0, 2204, and 6230 ppm, respectively.

consume the initial molecules to low polymers, then transform the liquid products into solid products, and finally, produce more highly polymerized coke. Differences in product would be unarguably enlarged, and the more reactive quinoline insoluble substances (some solid products and coke) would lead to uneven and disordered structures.

3.3. SOs with varying N concentration and their thermal stability

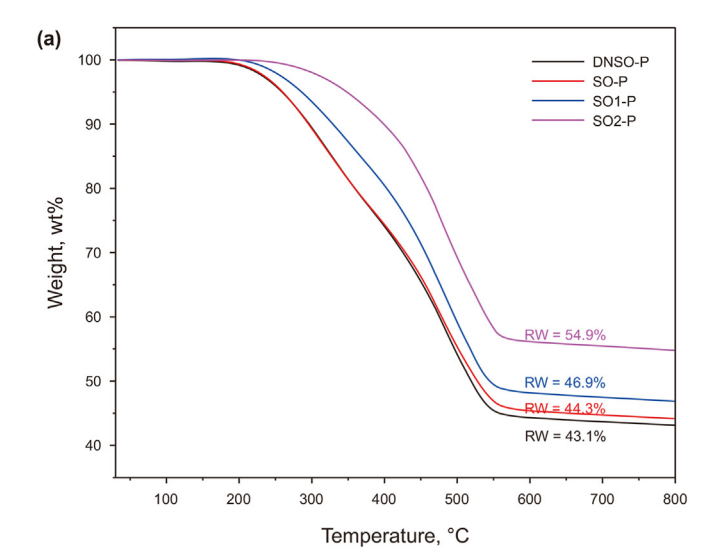
Based on the results of MD, it is necessary to investigate the influence of nitrogen on the thermal treatment progress and the properties of MCMB in the experiment. Therefore, four SOs containing different nitrogen content were prepared by extraction denitrification and blending of SO and recovery nitrogen-rich extractive phase oil. Their compositions were listed in Table 1. The molecular dynamics simulation of extractive denitrification was carried out, and the results were presented in Text S1, Figs. S3 and S4. It is proven that compounds of PEG2000 and water specifically interact with NC-PAH, other oil molecules were slightly affected due to the lipophobicity of water. Element composition and group composition change few except nitrogen. Due to the original SO was cut tail slurry oil at 500 °C, no asphaltenes were detected, and the sulfur contents were close to the standard 7000 ppm. Therefore, the influences of sulfur and asphaltenes could be ignored.

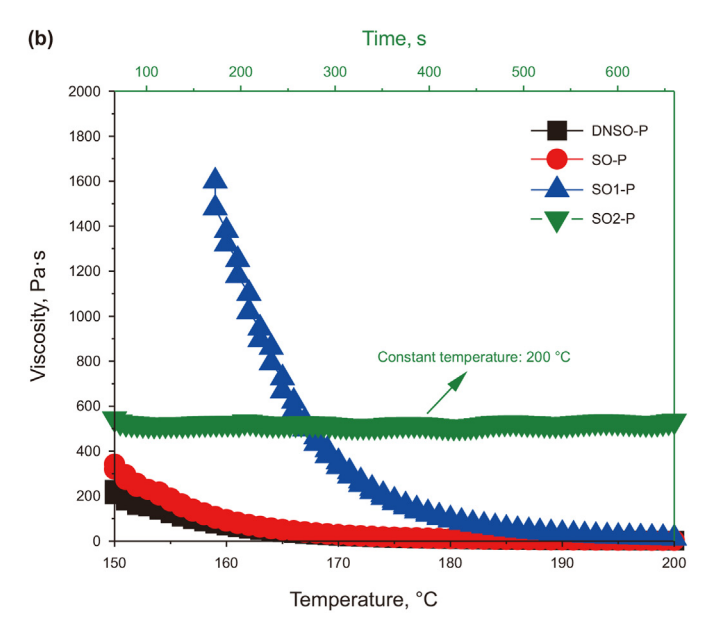
Pitches derived from SOs after 4 h of heat treatment were labeled as DNSO-P, SO-P, SO1-P, and SO2-P, respectively. Firstly, the system viscosity, TG, coke value, and quinoline insoluble substance (Fig. 4) were measured to explore what would happen in the early time when the nitrogen content increased. With increasing nitrogen content (NC), the thermal weight loss rate of pitches descended apparantly, and the residue weight (RW) elevated exponentially $(RW = 0.069 \times exp (NC/615.6) + 43.2)$, as shown in Fig. 4(a). It indicates the existence of the NC-PAH accelerated heat polymerization reaction and produced more reactive and highly condensed solid and coke products, then the system got stuck in the reaction acceleration vicious circle, which corresponds to the results of MD. System viscosity was detected by an rotational rheometer with a temperature limit of 200 °C, so the SO2-P with a high soft point was measured at the constant temperature (200 °C). The system viscosity of pitches also elevated non-linearly with NC, especially when the NC reached over 1500 ppm (Fig. 4(b)). The CV and QI both increased with NC, ranging from 57.6 to 66.1 wt% and 3.91 to 19.6 wt%, respectively (Fig. 4(c)). High reactivity of NC-PAH promoted the free radical reaction, so that more highly aggregated products arose and led to higher viscosity in a short time. Therefore, there was not enough time for the ordered rearrangement of aromatic layers. Jiao et al. (2020) investigated the effect of olefins on the development of the mesophase. Similar to the role of NC-PAH, olefins, as reactive substances, are more prone to produce free

 Table 1

 Elemental composition and group (SARA) analysis of SOs.

	SO	DNSO	SO1	SO2	
Elemental composition					
C, wt%	89.98	90.35	90.03	90.72	
H, wt%	7.83	7.97	8.00	7.51	
N, ppm	1475.1	482.1	2474.2	3158.9	
S, ppm	7672.5	7344.6	7614.2	7769.6	
Group analysis, wt%					
Saturates	7.8	7.9	7.7	6.3	
Aromatics	79.7	80.2	80.1	80.9	
Resins	12.5	11.9	12.2	12.8	
Asphaltenes	< 0.01	< 0.01	< 0.01	< 0.01	





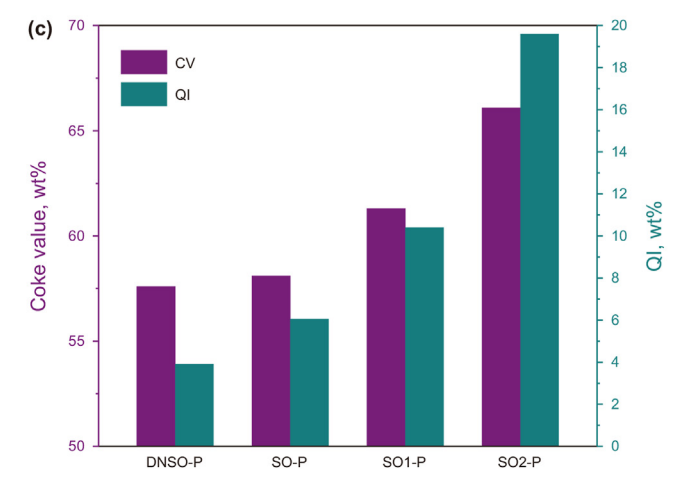


Fig. 4. Properties of pitches derived from SOs with varying nitrogen content were detected. **(a)** The thermal weight loss curves were compared, with the residue weight (RW) of pitches at 800 °C explicitly indicated. Viscosity and temperature curves were plotted in **(b)**, and the green point plot is measured at a constant 200 °C. The coke value and QI were shown in **(c)**.

radicals, which promote the polycondensation reaction, thus affecting the preparation of mesophase pitch. The type and content of olefins significantly influence the thermal stability of the slurry oil. A higher olefin content promotes increased coke formation during the early stages of the thermal condensation process. The presence of conjugated olefins accelerates the emergence of domain structures, with coarse-grained mosaic structures also interspersed in them. Therefore, NC-PAH and olefins, which have

substantially higher radical reactivity than ordinary PAH, must be eliminated to maintain the thermal stability of SO while preparing the mesophase.

The raised polarity and reactivity of NC-PAH in comparison to regular PAH may be examined in further depth using theoretical calculations and wave function investigations, revealing the mechanism by which the high nitrogen content leads to low thermal stability. Fig. 5(a) illustrates the distribution of the electrostatic

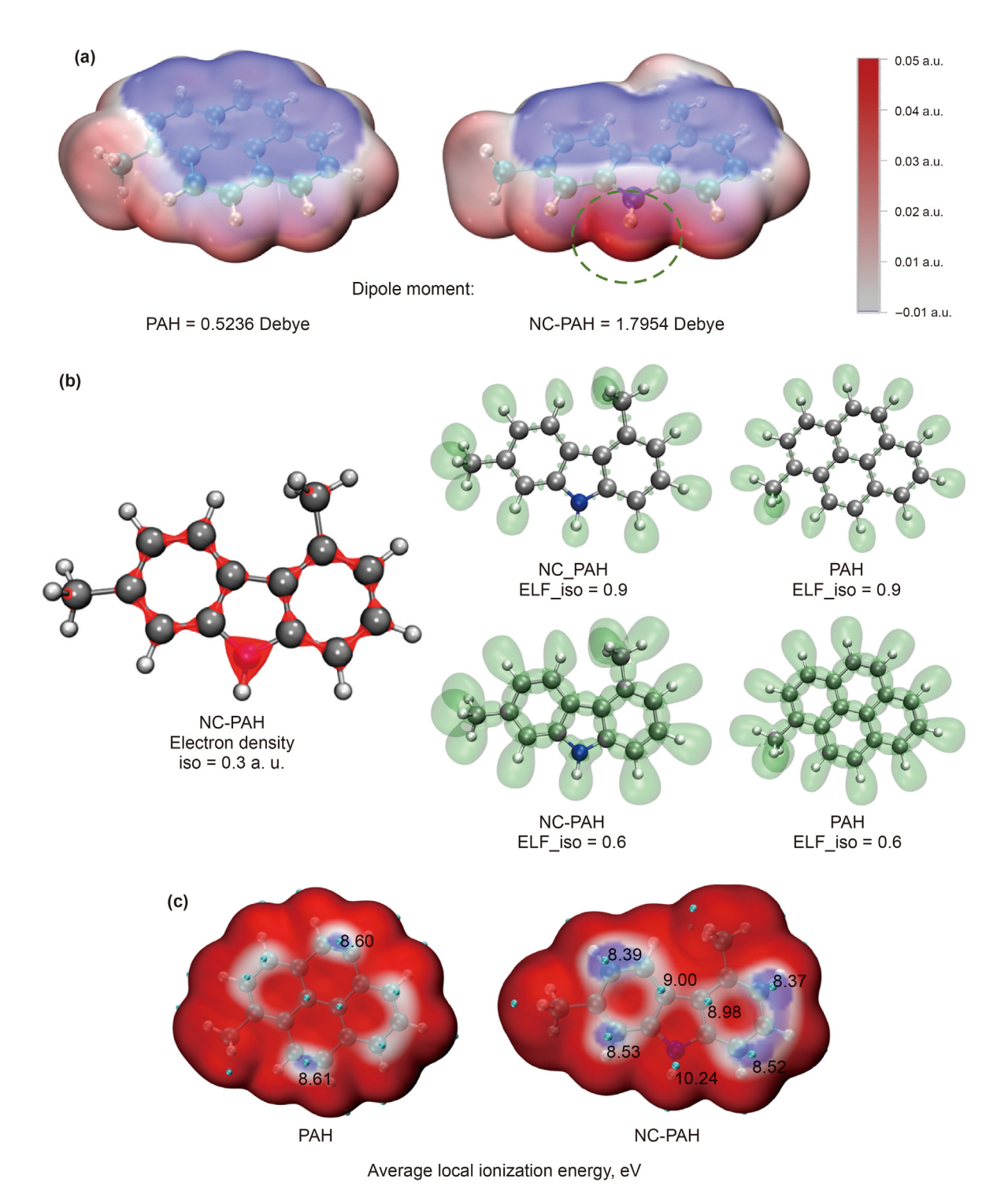


Fig. 5. Polarity and reactivity studies of PAH and NC-PAH. (a) Illustrates the electrostatic potential mapped onto the Van der Waals surface. (b) Presents the electron density isosurfaces (left panel) of NC-PAH and electron localization function (ELF) isosurfaces (right panel) for NC-PAH and PAH. The average localized ionization energy (ALIE) of PAH and NC-PAH is displayed in (c) on an isosurface with an electron density of 0.0005 a. u. Cyan spheres are used to accentuate regions with minimum values.

potential over the van der Waals surface, with the colors at different depths representing different values of the electrostatic potential. It appears that NC-PAH has a higher electrostatic potential locally due to the addition of N atoms, which increases the difference in the distribution of electrostatic potential and the molecule polarity, for instance, the dipole moments of PAH and NC-PAH are 0.5236 and 1.7954 Debye, respectively. The higher polarity results in the polarity effect replacing the π - π parallel stacking effect as the dominant effect during the stacking of aromatic layers, which is more likely to generate a disordered carbon layer structure (Fig. 6). The electron density isosurface map of NC-PAH on the left side of Fig. 5(b) reveals a larger region of isosurfaces around the nitrogen atom, which is a manifestation of the lone pair of electrons. The presence of lone pairs of electrons alters the electronic properties of NC-PAH and thus affects the radical reactivity, which can be examined in terms of the electron localization function (ELF) and the average localized ionization energy (ALIE). The ELF is a threedimensional real-space function with values between 0 and 1. Larger ELFs enclose regions where the electrons are more localized. For example, at an isosurface value of 0.9, only the σ covalent bond region of C-H (N-H) exhibits a distinct isosurface region (Fig. 5(b)). When the value of the isosurface is 0.6, the region surrounded by the isosurface has a smaller locality, and the electrons are delocalization in a certain region. From the ELF isosurface map with an isosurface value of 0.6 (Fig. 5(b)), it can be seen that the lone pair of electrons of the nitrogen atom of NC-PAH participates in the delocalized conjugation of the π -electrons of the aromatic rings, which increases the electron density of the neighboring and paraaromatic carbons, leading to an increase in the polarity and easier participation in the free radical reaction. In addition, the generation of free radicals by NC-PAH can stabilize the radical intermediates by dispersing the electron cloud of the radicals through lone-pair electron and conjugation effects, thus lowering the energy barrier of the radical reaction. The ALIE can be used as a measure of the binding ability of electrons at different positions of the molecule. The smaller the ALIE value, the weaker the binding ability of electrons and the easier it is to take part in the free radical reaction. As shown in Fig. 5(c), the ALIE values at the neighboring and para-C atoms of the C atom connected to the N atom of the NC-PAH molecule are the smallest, 8.37 and 8.52 eV, respectively. These results indicated that NC-PAH was more prone to free radical reaction at these sites, and the activity was higher than that of PAH. In the whole, the electronic properties of NC-PAHs make them more likely to participate in primary radical reactions, initiation, and growth of chains (Fig. 6). The stability of the NC-PAH radical increases the polymerization activity and raises the chain development period by lowering the probability of chain termination (Fig. 6). According to the above analyses, it is explained from the underlying mechanism why more highly polymerized products are generated in nitrogen-rich systems, whether in MD or thermal stability experiments.

3.4. Effect of NC-PAH on morphology of mesophase pitch

According to investigation of MD with ReaxFF and thermal stability of SOs, NC-PAH would enlarge the disparity of reaction progress and produce considerable solid and coke products, so that low viscosity reaction time was not enough and undesirable components such as QI generated. For studying what would happen to the morphology of mesophase pitch, optical structures, observed by a polarized optical microscope, of pitches derived from SOs with varying NC after 8 h heat treatment were shown in Fig. 7. Under orthogonal polarized light, the ordered anisotropic structures present the bright fields, while the disordered isotropic structures are in the dark (Brooks and Taylor, 1965). The anisotropic structure refers to the ordered arrangement of carbon layers that provided the channels and spaces for lithium-ions. Images were observed at different places of a sample under the same enlargement factor (such as Fig. 7(b3) and (b4), (c1) and (c2), etc.) due to the nonuniformity of samples prepared from SO with high NC.

Pitch prepared with DNSO in Fig. 7(a1)—(a4) contained abundant spheroidal mesophase with particle size ranges from 10 to 40 μ m in every sample. The particle size is fairly uniform compared with mesophase pitches in Fig. 7(b1)—(b4). This appropriate

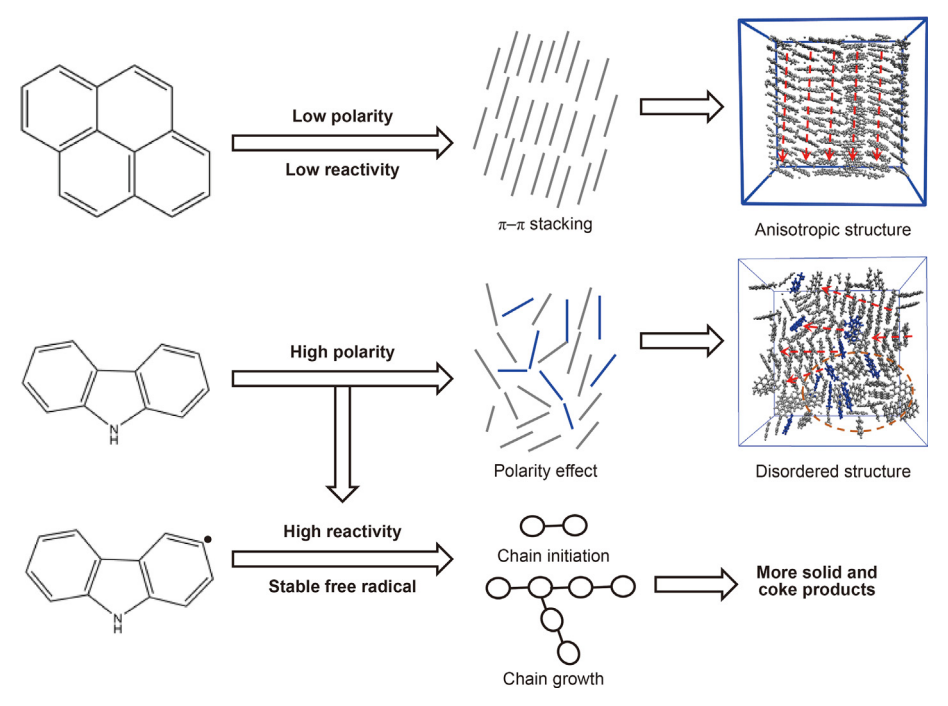


Fig. 6. Schematic diagram of differences in thermal polycondensation properties between PAH and NC-PAH.

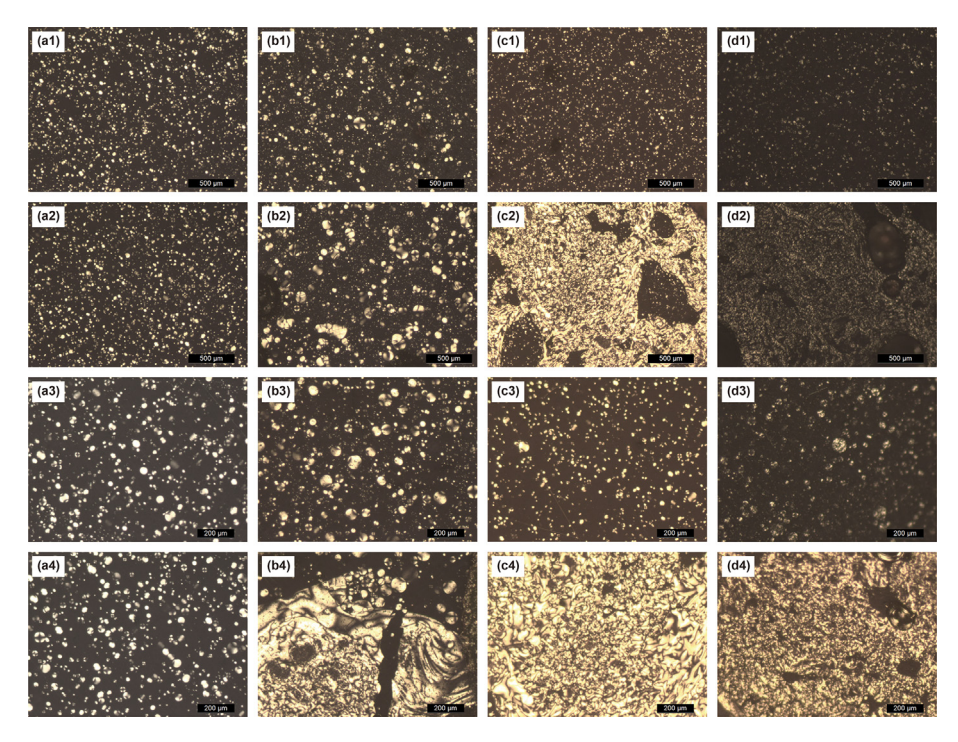


Fig. 7. Optical micrographs of mesophase pitch prepared at 430 °C for 8 h with DNSO ((a1)-(a4)), SO ((b1)-(b4)), SO ((c1)-(c4)), and SO2 ((d1)-(d4)).

particle distribution is positive for close-packing of MCMB. Some big beads (over 100 μm) appeared, and mesophase sphere coalescence could be observed in Fig. 7(b1)-(b4). What is more, bulk mesophase started to form due to the coalescence and deformation of mesophase spheres (Fig. 7(b4)). Obviously, the NC-PAHs with high reactivity accelerated the reaction and led to big beads and bulk mesophase. A certain amount of nitrogen in SO promoted the reaction of progress in some areas and resulted in coarse-grained mosaic structures (Fig. 7(b4)), which destroyed large domain structures. When the NC further increased, the ratio of small domain and mosaic structures elevated while few big spheres over 100 μm existed (Fig. 7(c) and (d)). It seems that most big spheres have merged and transformed to bulk mesophase. The considerable small domain and mosaic structures can be attributed to the QIs and high viscosity, which obstacle the parallel arrangement of aromatic layers and orderly development of mesophases. MCMB with uniform particle size could also be obtained by removing impurities

and optimizing components through complex processes such as hydrogenation, distillation, and extraction (Zhang et al., 2019; Guo et al., 2020b; Jiao et al., 2020, 2021). The particle size uniformity and sphericity of MCMB prepared by extractive denitrification were comparable to the best products in the literature. The pitches prepared from high nitrogen content SO were similar to those prepared from raw feedstocks or heavier components of feedstocks in the literature. For instance, the bead coalescence and mosaic structures embedded in the domain structure became the main structure. Although different methods were carried out, the purposes were both to remove components with polarity and free radical reactivity higher than the ordinary PAHs. In summary, similar to asphaltene and olefins, NC-PAH significantly affects the morphology and structure of products due to its own properties.

More details of surface morphology and isotropic substances can be analyzed by scanning electron microscopy (SEM), and SEM images are presented in Fig. 8. After denitrification, MCMBs with

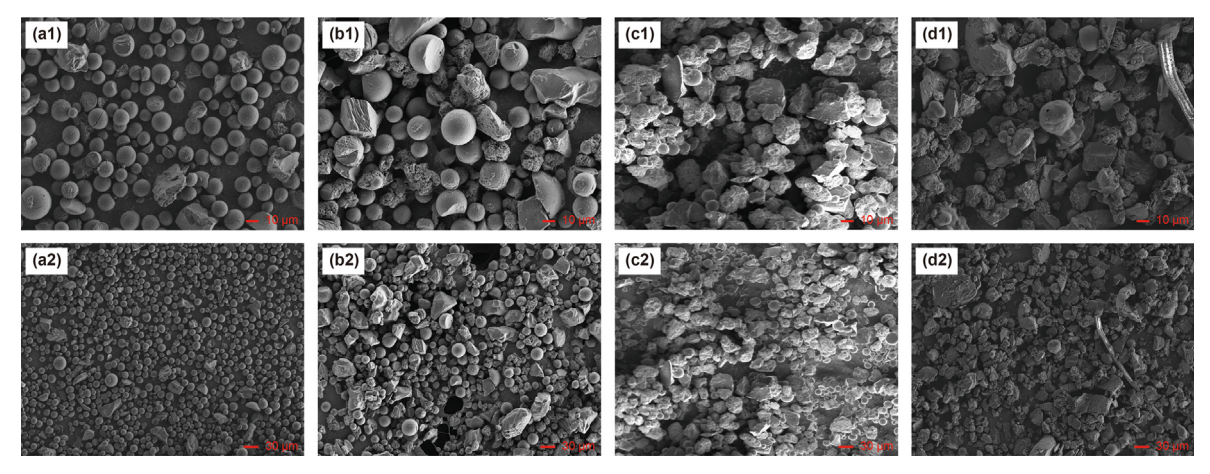


Fig. 8. SEM images of MCMB prepared at 430 °C for 8 h with DNSO ((a1) and (a2)), SO ((b1) and (b2)), SO1 ((c1) and (c2)), and SO2 ((d1) and (d2)).

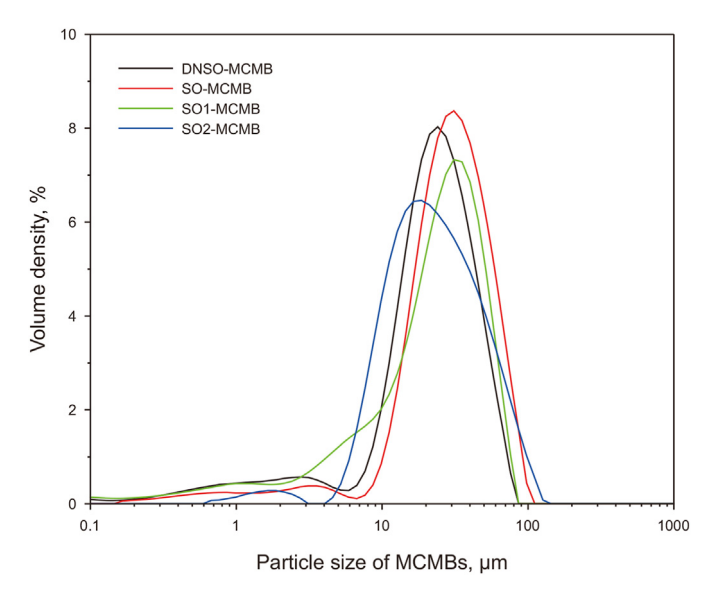
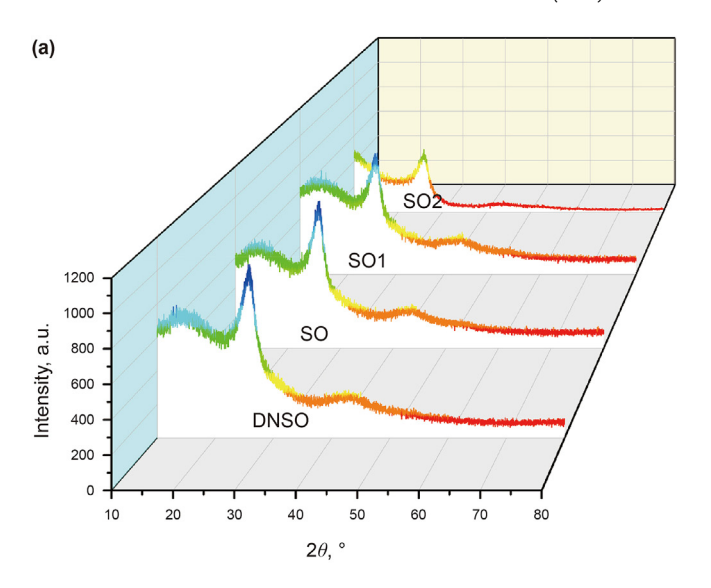
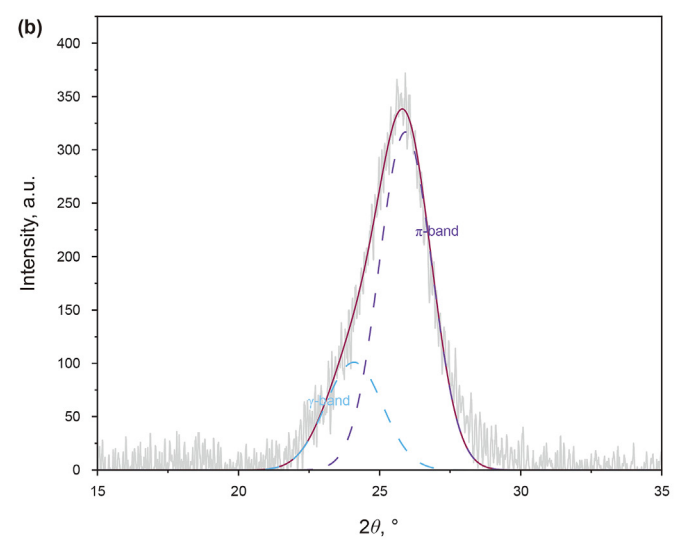


Fig. 9. Particle size distributions of MCMBs are detected by laser particle size analyzer.

uniform particle size were obtained through thermal treatment (Fig. 8(a1) and (a2)). Smooth surfaces refer to homogeneous nucleation with few solid QIs. In the absence of NC-PAH, the thermal polycondensation reaction proceeded steadily and uniformly. As revealed by molecular dynamics simulations, the system without NC-PAH has a slower rate of molecular consumption and produces fewer highly polymerized coke products. The SO with more NC-PAHs produced more bulk products and small carbon particles (<200 nm) parceling spheres and lumps (Fig. 8(b1) and (b2)). Bulk products became the major products after the NC further elevated (Fig. 8(c1) and (c2)). A lot of structures of disordered accumulation polycondensation doped in products prepared by SO1 and SO2. High NC also led to a low degree of sphericity. The lumpy products and disordered structure can correspond to the large amount of solid and coke products produced in simulation systems b and c. In the initial reaction stage, highly polar NC-PAHs disrupt the π - π stacking of the aromatic layers (Figs. 5 and 6), and the resulting QIs (Fig. 4) serve as the cores for the development of a more disordered carbon layer structure. In the middle and late stages of the reaction, the physical process of merge and rearrangement of the mesophases is limited by the high viscosity (Fig. 4) of the system. As a result, the products prepared from SOs with high nitrogen content have poor morphological homogeneity and structural ordering. It is demonstrated that denitrification is necessary for MCMB with uniform particles and excellent sphericity.

The particle distributions of MCMBs are displayed in Fig. 9. The particle size distribution range of MCMB prepared by DNSO was narrow, the average particle size by volume was 26.0 μm , and the volume-based cumulative distribution diameter at 90% (Dv (90)) was 49.8 μm . The particle size of SO-MCMB was higher than that of DNSO-MCMB, with an average volume particle size of 31.5 μm and Dv (90) of 64.5 μm . The results showed that the presence of NC-PAH accelerated the development of mesophase, which was related to the polarity and the reactivity of free radicals of NC-PAH. The domain structure embedded with considerable mosaic structure could be seen in the polarized light microscope (Fig. 7(b)), which was not reflected in SEM and particle size distribution. This might be due to the fact that large bulk products were dispersed into small





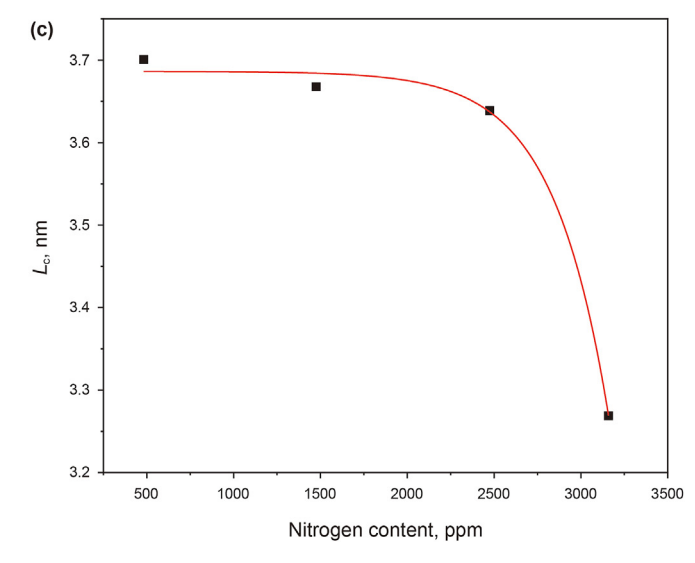


Fig. 10. (a) XRD spectra of MCMBs prepared with DNSO, SO, SO1, and SO2, the intensity varies by the colors from red to blue. (b) The broad lump near 26° was divided into γ -band and π -band. (c) Stack height was plotted against nitrogen content.

 Table 2

 Structure parameters of MCMBs prepared with SOs.

Sample	2 <i>θ</i> _π , °	FWHM, °	d ₀₀₂ , nm	L _c , nm	N
DNSO	25.916	2.180	0.344	3.701	11.764
SO	25.847	2.199	0.345	3.668	11.642
SO1	25.819	2.216	0.345	3.639	11.547
SO2	25.811	2.467	0.345	3.269	10.472

pieces during pyridine extraction. When the nitrogen content was further raised, the domain structures in SO1-MCMB were divided by more mosaic structures. Therefore, the large bulk products are dispersed into smaller bulk particles during the pyridine extraction and the particle size of SO1-MCMB was somewhat smaller than that of SO-MCMB. Due to the significant disparity in reaction progress, there appeared to be some phase separation between the solid product and the mother liquor during the reaction. The mother liquor containing less PAH produced small particle size MCMB (1–10 μm). The small beads in the mother liquor grow, and the bulk products increase further in SO2-MCMB, and the distribution of the products further disperses.

3.5. Crystalline structure analysis of MCMB

High reactivity of NC-PAH not only led to high viscosity, QI, and morphology discrepancy but also affected to a great extent the crystalline structures of MCMB, which play an important role on the properties of lithium-ion batteries. Crystalline structures of MCMBs were researched through XRD, and XRD spectra were presented in Fig. 10(a). MCMBs prepared with SOs with varying NC exhibit various intensity for characteristic peak of d_{002} at near 26°. It indicates that the obtained MCMBs possess different degrees of crystallinities. As presented in Fig. 10(a), the (002) peak turns short and dispersive when the nitrogen content increases, which means

that the structure of aromatic layers got worse. When NC-PAH exists, the polarity effect replaces the π - π conjugation effect and breaks the ordered stacking of aromatic layers. As reported in the literature (Balachandran and Ag, 2012; Zhu et al., 2019), the broad hump of (002) of carbonaceous materials is the superposition of γ band and π -band at the diffraction peak position near 20° and 26° Fig. 10(b), (Fig. S5). Actually, the key structural parameters such as interlayer spacing (d_{002}) , stack height (L_c) , and parallel layer number (N) can be calculated according to Eqs. (1)–(3) (Warren, 1941; Short and Walker, 1963). The specific crystalline particle sizes were calculated and listed in Table 2. The layer spacing increased, and stack height (3.701–3.269) and parallel layer number (11.764–10.472) descended with the increase of nitrogen content. According to the literature, after the removal of resin and asphaltene by hydrogenation and distillation, the prepared MCMB crystal size L_c increased from 2.50 to about 3.25 and N increased from 8.10 to about 10.15 (Guo et al., 2020b). The L_c of mesophase pitch made by hydrogenated SO and SOs with various olefin additions ranged from 2.91 to 3.27 when the influence of olefin was examined, and the N varied from 9.36 to 10.40 (Jiao et al., 2020). The influence of nitrogen content on stack height is approximately exponential (Fig. 10(c)), like the influence on viscosity, QI, and thermal residue weight (Fig. 4). These negative effects perform a vicious accumulation and vicious cycle because the thermal condensation reaction and mesophase development are affected by the products generated in the early stage and system viscosity besides initial content of NC-PAH. It is clear that NC-PAH has a significant effect on the crystallite size of the mesophase, in addition to the undesirable components such as olefins, resins, asphaltenes, and other polar, highly radical-reactive components.

$$d_{002} = \lambda / (2 \times \sin \theta_{\pi}) \tag{1}$$

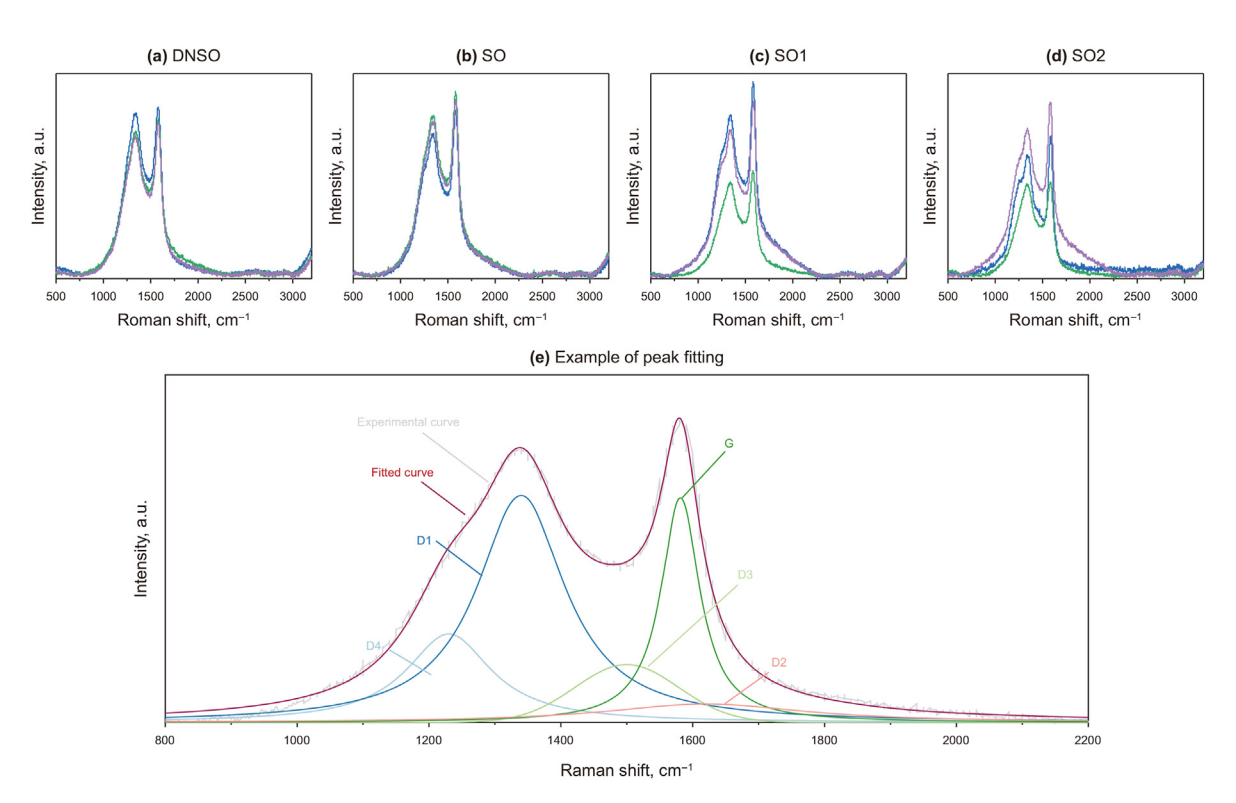


Fig. 11. Raman spectra of (a) DNSO-MCMB, (b) SO-MCMB, (c) SO1-MCMB, and (d) SO2-MCMB at three detecting points per sample. (e) Curve-fitting image of one Raman spectra of DNSO-MCMB. More curve-fitting results are plotted in Fig. S6.

Table 3Raman spectra fitting standards and vibration mode reported by literature.

Band	Raman shift, cm ⁻¹	Vibration mode
G	-1580	Ideal graphitic lattice
D1	-1350	Disordered graphitic lattice (graphene layer edges)
D2	-1620	Disordered graphitic lattice (surface graphene layers)
D3	-1500	Amorphous carbon
D4	-1200	Disordered graphitic lattice (polyenes, impurities)

$$L_{\rm C} = K_{\rm C} \times \lambda / (\beta_{\rm \pi} \times \cos \theta_{\rm \pi}) \tag{2}$$

$$N = 1 + L_{\rm c}/d_{002} \tag{3}$$

where λ is X-ray wavelength (0.15418 nm), $K_{\rm c}=0.89$, β_{π} means the full width at half maximum (FWHM) of π -band, and θ_{π} means the diffraction angle of π -band.

The average crystalline particle structure was analyzed by XRD. However, the investigation using a polarized optical microscope and SEM revealed that morphology differences in the same sample appeared when the nitrogen content increased. Therefore, Raman spectra were employed to explore the structure of samples at different areas. As presented in Fig. 11(a)-(d), two prominent peaks at near $1360~\text{cm}^{-1}$ (D band) and $1580~\text{cm}^{-1}$ (G band) were discovered on the spectra. Though similar types of peaks of MCMBs were observed, the variances of intensity and width existed, especially for MCMBs derived from SO1 and SO2. These differences confirm that NC-PAH brought variances of structure besides morphology. Furthermore, in order to study the evolution of structure disorder degree with elevation of nitrogen content, Raman spectra were divided into five bands according to the Raman peak fitting standards (Table 3) (Sadezky et al., 2005). As shown in Fig. 11(e) and Fig. S6, the major D and G bands were fitted with five peaks (D1, D2, D3, D4, and G), and the area of peaks was calculated by integration. The G peak represented the vibration of the ideal graphite crystal structure (Table 3). Hence, the area ratio (A_G/A_{all}) is employed to estimate the degree of graphitization of MCMBs (Fig. 12). The degrees of graphitization of MCMBs derived from DNSO and SO are more uniform than MCMBs prepared with SO1 and SO2, and the mean degree of graphitization of DNSO-MCMB (20.58%) is higher than SO-MCMB (18.43%). Extremely low degrees of graphitization appear in SO1-MCMB (16.43%) and SO2-

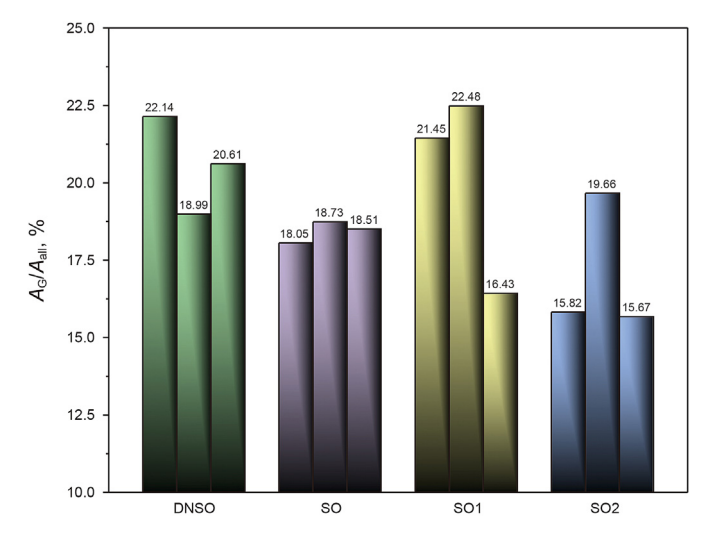


Fig. 12. Degree of graphitization ($A_{\rm G}/A_{\rm all}$) of MCMBs prepared with DNSO, SO, SO1, and SO2.

MCMB (15.67%). Three random points were chosen for each sample, and the raw data was presented, so high degrees of graphitization can also be found in SO1-MCMB and SO2-MCMB. The reduced graphitization can be explained by the fact that NC-PAH and QI affect the parallel stacking of aromatic layers. Gong et al. (2022) added various content carbon black into SO as the nucleation center, the A_G/A_{all} elevated from 17.7% to 18.03% then descended to 14.79%. It was verified that nucleation center such as QI and carbon black promoted growth of microbeads and lead to disordered structure. The graphitization variability of the products at high nitrogen content seems to be related to phase separation due to high system viscosity, besides NC-PAH and QI. The highly polymerized products separate from the low polymerization products due to the density difference. The high viscosity restricts the material exchange, and the reaction gap is further widened. The low polymerization product phase gently develops into a high graphitization mesophase, while the high polymerization product phase generates a mosaic structure and disordered coke. It indicates that NC-PAH will lead to more structural disorder degree and structure difference.

4. Conclusions

Through the investigation of pyrolysis behaviors utilizing MD with ReaxFF, it is confirmed that methyl side chains affect the thermal radical reaction activity more than the number of aromatic rings. NC-PAH is clearly more reactive than PAH, and will accelerate the consumption rate of other PAHs. Simulation systems with NC-PAH tend to produce more highly condensed solid and coke products, which corresponds to QI and high viscosity in the experiment. The thermal stability descends exponentially, especially over 1475 ppm, the residue weight (800 °C, N₂), viscosity, QI, and CV elevated remarkably. These are detrimental to the ordered arrangement of aromatic layers and mass and heat transfer. Through denitrification, the nitrogen content reached lower than 500 ppm, and the DNSO-MCMB has small and uniform particles with excellently spherical shape. The small domain and mosaic structures and lump substances begin to become the major products with the increase of nitrogen content (over 1500 ppm). Furthermore, the average crystalline particle size and graphitization degree decrease, and the structure distribution uniformity gets worse when the nitrogen content increases, particularly over 1500 ppm. This work suggests that the nitrogen content of SO should be limited under 1500 ppm for decent ordered structure, and lower nitrogen content (500 ppm) is necessary for uniform, ordered, and spherical MCMBs. Nitrogen-rich extraction recovers oils are suitable for the preparation of more disordered nitrogen doped hard carbon materials.

CRediT authorship contribution statement

Xing-Guo Wei: Writing — original draft, Visualization, Validation, Resources, Methodology, Investigation, Data curation, Conceptualization. **Yuan-Qin Zhang:** Writing — review & editing, Validation, Data curation, Conceptualization. **Ling-Rui Cui:** Writing

review & editing, Validation, Funding acquisition. Cao Liu:
 Writing — review & editing, Validation, Conceptualization. Jian
 Huang: Writing — review & editing, Validation, Conceptualization.
 Fa-Hai Cao: Writing — review & editing, Supervision, Project administration, Funding acquisition.

Declaration of competing interest

The authors declare the following financial interests/personal relationships which may be considered as potential competing interests: Lingrui Cui reports financial support was provided by National Natural Science Foundation of China. If there are other authors, they declare that they have no known competing financial interests or personal relationships that could have appeared to influence the work reported in this paper.

Acknowledgements

The authors thank Research Center of Analysis and Test of East China University of Science and Technology for the help on the characterizations (elemental composition, S/N analyzer, group analysis, polarized light optical microscopy, XRD). The authors extend their gratitude to Mr. Li Ning from Shiyanjia Lab (www.shiyanjia.com) for providing invaluable assistance with the TG, SEM, and Raman analysis. The authors thank Super Computing Network (SCNet, www.scnet.cn, AC.sugon.com) for providing computational resources (Gaussian, Gromacs, and LAMMPS). The authors acknowledge the support of National Natural Science Foundation of P. R. China (22308104).

Appendix A. Supplementary data

Supplementary data to this article can be found online at https://doi.org/10.1016/j.petsci.2025.03.031.

References

- Abraham, M.J., Murtola, T., Schulz, R., et al., 2015. GROMACS: high performance molecular simulations through multi-level parallelism from laptops to supercomputers. SoftwareX 1–2, 19–25. https://doi.org/10.1016/j.softx.2015.06.001.
- Ayyappan, S., Choudhary, T.V., 2016. Slurry Oil Upgrading while Preserving Aromatic Content, US9375656B2.
- Balachandran, M., Ag, K., 2012. Study of stacking structure of amorphous carbon by X-ray diffraction technique. Int. J. Electrochem. Sci. 7, 3127–3134. https://doi.org/10.1016/S1452-3981(23)13940-X.
- Brooks, J., Taylor, G., 1965. The formation of graphitizing carbons from the liquid phase. Carbon 3, 185–193. https://doi.org/10.1016/0008-6223(65)90047-3.
- Castro-Marcano, F., Kamat, A.M., Russo, M.F., et al., 2012. Combustion of an Illinois No. 6 coal char simulated using an atomistic char representation and the ReaxFF reactive force field. Combust. Flame 159, 1272–1285. https://doi.org/10.1016/ j.combustflame.2011.10.022.
- Chávez Thielemann, H., Cardellini, A., Fasano, M., et al., 2019. From GROMACS to LAMMPS: gro2LAM. J. Mol. Model. 25, 147. https://doi.org/10.1007/s00894-019-
- Darden, T., York, D., Pedersen, L., 1993. Particle mesh Ewald: an N·log(N) method for Ewald sums in large systems. J. Chem. Phys. 98, 10089—10092. https://doi.org/10.1063/1.464397.
- Frisch, M.J., Trucks, G.W., Schlegel, H.B., et al., 2013. Gaussian 09, Revision E.01. Gaussian, Inc., Wallingford CT. Gong, X., Lou, B., Yu, R., et al., 2021. Carbonization of mesocarbon microbeads
- Gong, X., Lou, B., Yu, R., et al., 2021. Carbonization of mesocarbon microbeads prepared from mesophase pitch with different anisotropic contents and their application in lithium-ion batteries. Fuel Process. Technol. 217, 106832. https:// doi.org/10.1016/j.fuproc.2021.106832.
- Gong, X., Guo, S., Ding, Y., et al., 2022. Preparation of mesocarbon microbeads as anode material for lithium-ion battery by co-carbonization of FCC decant oil and conductive carbon black. Fuel Process Tech. 227, 107110. https://doi.org/10.1016/j.fuproc.2021.107110.
- Grimme, S., 2006. Semiempirical GGA-type density functional constructed with a long-range dispersion correction. J. Comput. Chem. 27, 1787–1799. https://doi.org/10.1002/jcc.20495.
- Guo, A., Wang, F., Jiao, S., et al., 2020a. Mesophase pitch production from FCC slurry oil: optimizing compositions and properties of the carbonization feedstock by

- slurry-bed hydrotreating coupled with distillation. Fuel 262, 116639. https://doi.org/10.1016/j.fuel.2019.116639.
- Guo, A., Wang, F., Jiao, S., et al., 2020b. Preparation of mesocarbon microbeads as anode material for lithium-ion battery by thermal polymerization of a distillate fraction from an FCC slurry oil after hydrofining with suspended catalyst. Fuel 276, 118037. https://doi.org/10.1016/j.fuel.2020.118037.
- Guo, Y., He, H., Liu, X., et al., 2021. Ring-opening and hydrodenitrogenation of indole under hydrothermal conditions over Ni, Pt, Ru, and Ni-Ru bimetallic catalysts. Chem. Eng. I. 406. 126853. https://doi.org/10.1016/i.cei.2020.126853.
- Haratake, M., Hidaka, S., Ono, M., et al., 2007. Preparation of an ion-exchangeable polymer bead wrapped with bilayer membrane structures for high performance liquid chromatography. Anal. Chim. Acta 589, 76–83. https://doi.org/10.1016/j.aca.2007.02.047.
- Hoover, W.G., 1985. Canonical dynamics: equilibrium phase-space distributions. Phys. Rev. A 31, 1695–1697. https://doi.org/10.1103/PhysRevA.31.1695.
- Jana, A., Zhu, T., Wang, Y., et al., 2022. Atoms to fibers: identifying novel processing methods in the synthesis of pitch-based carbon fibers. Sci. Adv. 8, eabn1905. https://doi.org/10.1126/sciady.abn1905.
- Jian, C., Adams, J.J., Grossman, J.C., et al., 2021. Carbon fiber synthesis from pitch: insights from ReaxFF based molecular dynamics simulations. Carbon 176, 569–579. https://doi.org/10.1016/j.carbon.2021.01.151.
- Jian, C., Merchant, S., Zang, X., et al., 2019. Structural evolutions of small aromatic mixtures under extreme temperature conditions: insights from ReaxFF molecular dynamics investigations. Carbon 155, 309–319. https://doi.org/10.1016/i.carbon.2019.08.048.
- Jiao, S., Guo, A., Wang, F., et al., 2020. Effects of olefins on mesophase pitch prepared from fluidized catalytic cracking decant oil. Fuel 262, 116671. https://doi.org/ 10.1016/i.fuel.2019.116671.
- Jiao, S., Guo, A., Wang, F., et al., 2021. Sequential pretreatments of an FCC slurry oil sample for preparation of feedstocks for high-value solid carbon materials. Fuel 285, 119169. https://doi.org/10.1016/j.fuel.2020.119169.
- Jin, L.E., Cao, Q., Li, J., et al., 2011. Sulfur removal in coal tar pitch by oxidation with hydrogen peroxide catalyzed by trichloroacetic acid and ultrasonic waves. Fuel 90, 3456–3460. https://doi.org/10.1016/j.fuel.2011.06.047.
- Kim, S.W., Lee, J.W., Koh, J.S., et al., 2012. Formation and characterization of deposits in cyclone dipleg of a commercial residue fluid catalytic cracking reactor. Ind. Eng. Chem. Res. 51, 14279—14288. https://doi.org/10.1021/ie301864x.
- Li, M., Liu, D., Men, Z., et al., 2018. Effects of different extracted components from petroleum pitch on mesophase development. Fuel 222, 617–626. https:// doi.org/10.1016/j.fuel.2018.03.011.
- Li, T., Wang, C., Liu, X., et al., 2005. Characteristics of mesocarbon microbeads generated from a coal tar pitch with addition of micro-alumina powder. Fuel Process. Technol. 87, 77–83. https://doi.org/10.1016/j.fuproc.2005.07.003.
- Li, W., Chen, Y., Zhang, L., et al., 2016. Supercritical fluid extraction of fluid catalytic cracking slurry oil: bulk property and molecular composition of narrow fractions. Energy & Fuels 30, 10064–10071. https://doi.org/10.1021/acs.energyfuels.6b01132.
- Liu, X., Guo, Y., He, H., et al., 2022. A comprehensive study of indole catalytic hydrodenitrogenation under hydrothermal conditions. AIChE J. 68, e17531. https://doi.org/10.1002/aic.17531.
- Liu, X., Ding, S., Wei, Q., et al., 2021. DFT insights in to the hydrodenitrogenation behavior differences between indole and quinoline. Fuel 285, 119039. https:// doi.org/10.1016/j.fuel.2020.119039.
- Lu, T., Chen, F., 2012. Multiwfn: a multifunctional wavefunction analyzer. J. Comput. Chem. 33, 580–592. https://doi.org/10.1002/jcc.22885.
- Mochida, I., Sakanishi, K., Usuba, H., et al., 1991. Removal of basic nitrogen species in coal-tar pitch by metal sulphates supported on silica gel. Fuel 70, 761–764. https://doi.org/10.1016/0016-2361(91)90075-L.
- Mochida, I., Furuno, T., Fujitsu, H., et al., 1988. Hydrodesulphurization of needle coke in atmospheric hydrogen flow. Fuel 67, 678–681. https://doi.org/10.1016/0016-2361(88)90298-0.
- Nosé, S., 1984. A molecular dynamics method for simulations in the canonical ensemble. Mol. Phys. 52, 255–268. https://doi.org/10.1080/00268978400101201.
- Oi, S., Onishi, N., Yamada, Y., et al., 1978. Influence of organic sulfur compounds and metals on mesophase formation. Carbon 16, 445–452. https://doi.org/10.1016/0008-6223(78)90091-X.
- Radovic, L.R., 2005. The mechanism of CO₂ chemisorption on zigzag carbon active sites: a computational chemistry study. Carbon 43, 907–915. https://doi.org/ 10.1016/j.carbon.2004.11.011.
- Sadezky, A., Muckenhuber, H., Grothe, H., et al., 2005. Raman microspectroscopy of soot and related carbonaceous materials: spectral analysis and structural information. Carbon 43, 1731–1742. https://doi.org/10.1016/j.carbon.2005.02.018.
- Sanada, Y., Furuta, T., Kimura, H., et al., 1973. Formation of anisotropic mesophase from various carbonaceous materials in early stages of carbonization. Fuel 52, 143–148. https://doi.org/10.1016/0016-2361(73)90039-2.
- Schauperl, M., Nerenberg, P.S., Jang, H., et al., 2020. Non-bonded force field model with advanced restrained electrostatic potential charges (RESP2). Commun. Chem. 3, 44. https://doi.org/10.1038/s42004-020-0291-4.
- Short, M.A., Walker, P.L., 1963. Measurement of interlayer spacings and crystal sizes in turbostratic carbons. Carbon 1, 3–9. https://doi.org/10.1016/0008-6223(63) 90003-4.
- Song, X.N., Liu, D., Lou, B., et al., 2018. Removal of catalyst particles from fluid catalytic cracking slurry oil by the simultaneous addition of a flocculants and a

- weighting agent. Chem. Eng. Res. Des. 132, 686–696. https://doi.org/10.1016/
- Stukowski, A., 2010. Visualization and analysis of atomistic simulation data with OVITO—the Open Visualization Tool. Model. Simulat. Mater. Sci. Eng. 18, 015012. https://doi.org/10.1088/0965-0393/18/1/015012.
- Sun, W., Guo, S., Liu, Y., et al., 2022. The desulfurization of coal tar pitch with potassium permanganate oxidation method. Fuel 323, 124230. https://doi.org/10.1016/j.fuel.2022.124230.
- Taha, M., Lee, M.-J., 2013. TES buffer-induced phase separation of aqueous solutions of several water-miscible organic solvents at 298.15 K: Phase diagrams and molecular dynamic simulations. J. Chem. Phys. 138, 244501. https://doi.org/ 10.1063/1.4809995.
- Thompson, A.P., Aktulga, H.M., Berger, R., et al., 2022. Lammps—a flexible simulation tool for particle-based materials modeling at the atomic, meso, and continuum scales. Comput. Phys. Commun. 271, 108171. https://doi.org/10.1016/i.cpc.2021.108171.
- Trejo, F., Rana, M.S., Ancheyta, J., 2010. Thermogravimetric determination of coke from asphaltenes, resins and sediments and coking kinetics of heavy crude asphaltenes. Catal. Today 150, 272–278. https://doi.org/10.1016/j.cattod.2009.07.091.
- Vázquez-Garrido, I., López-Benítez, A., Berhault, G., et al., 2019. Effect of support on the acidity of NiMo/Al₂O₃-MgO and NiMo/TiO₂-Al₂O₃ catalysts and on the resulting competitive hydrodesulfurization/hydrodenitrogenation reactions. Fuel 236, 55–64. https://doi.org/10.1016/j.fuel.2018.08.053.
- Wang, J., Wang, W., Kollman, P.A., et al., 2006. Automatic atom type and bond type perception in molecular mechanical calculations. J. Mol. Graphics Modell. 25, 247–260. https://doi.org/10.1016/j.jmgm.2005.12.005.
- Wang, J., Wolf, R.M., Caldwell, J.W., et al., 2004. Development and testing of a general Amber force field. J. Comput. Chem. 25, 1157–1174. https://doi.org/ 10.1002/icc.20035.
- Wang, Y.C., Egashira, M., Ishida, S., et al., 1999a. Microstructure of mesocarbon microbeads prepared from synthetic isotropic naphthalene pitch in the presence of carbon black. Carbon 37, 307–314. https://doi.org/10.1016/S0008-6223(98)00179-1.
- Wang, Y.G., Chang, Y.C., Ishida, S., et al., 1999b. Stabilization and carbonization properties of mesocarbon microbeads (MCMB) prepared from a synthetic naphthalene isotropic pitch. Carbon 37, 969–976. https://doi.org/10.1016/S0008-6223(98)00292-9.
- Warren, B.E., 1941. X-ray diffraction in random layer lattices. Phys. Rev. 59, 693–698. https://doi.org/10.1103/PhysRev.59.693.

- Wei, X., Cui, L., Cen, L., et al., 2023. Effective electrostatic potential surface and aromatic affinity as quantitative guide for deep extraction denitrification from aromatic-rich oils. Sep. Purif. Technol. 330, 125476. https://doi.org/10.1016/i.seppur.2023.125476.
- Yan, W.W., Zong, Z.M., Li, Z.X., et al., 2020. Effective separation and purification of nitrogen-containing aromatics from the light portion of a high-temperature coal tar using choline chloride and malonic acid: experimental and molecular dynamics simulation. ACS Sustainable Chem. Eng. 8, 9464–9471. https:// doi.org/10.1021/acssuschemeng.0c02369.
- Yang, H., Wang, L., Zhou, H., et al., 2021. Reactive molecular dynamics simulation in the early stage of naphthalene carbonisation. Mol. Simul. 47, 1282–1289. https://doi.org/10.1080/08927022.2021.1967950.
- Yang, Y., Lin, Q., Huang, Y., et al., 2011. Efficient preparation of mesocarbon microbeads by pyrolysis of coal-tar pitch in the presence of rosin. J. Anal. Appl. Pyrolysis 91, 310—315. https://doi.org/10.1016/j.jaap.2011.03.005.
- Yin, Y., Chen, W., Wu, G., et al., 2021. Kinetics toward mechanism and real operation for ultra-deep hydrodesulfurization and hydrodenitrogenation of diesel. AlChE J. 67, e17188. https://doi.org/10.1002/aic.17188.
- Yu, R., Liu, D., Lou, B., et al., 2019. The effect of solvent extraction on petroleum pitch compositions and their pyrolysis behaviors. Fuel 247, 97–107. https://doi.org/ 10.1016/j.fuel.2019.03.041.
- Zang, X., Jian, C., Ingersoll, S., et al., 2020. Laser-engineered heavy hydrocarbons: old materials with new opportunities. Sci. Adv. 6, eaaz5231. https://doi.org/10.1126/sciady.aaz5231
- Zhang, D., Zhang, L., Fang, X., et al., 2019. Enhancement of mesocarbon microbead (MCMB) preparation through supercritical fluid extraction and fractionation. Fuel 237, 753—762. https://doi.org/10.1016/j.fuel.2018.10.054.
- Zhang, D., Zhang, L., Yu, Y., et al., 2018. Mesocarbon microbead production from fluid catalytic cracking slurry oil: improving performance through supercritical fluid extraction. Energy & Fuels 32, 12477—12485. https://doi.org/10.1021/acs.energyfuels.8b03498.
- Zhao, D., Liu, C., Wang, Y., et al., 2022. Ionic liquids design for efficient separation of anthracene and carbazole. Sep. Purif. Technol. 281, 119892. https://doi.org/ 10.1016/j.seppur.2021.119892.
- Zhong, M., Yan, J., Wu, H., et al., 2020. Multilayer graphene spheres generated from anthracite and semi-coke as anode materials for lithium-ion batteries. Fuel Process. Technol. 198, 106241. https://doi.org/10.1016/j.fuproc.2019.106241.
- Zhu, Y., Zhao, C., Xu, Y., et al., 2019. Preparation and characterization of coal pitch-based needle coke (Part I): the effects of aromatic index (fa) in refined coal pitch. Energy & Fuels 33, 3456—3464. https://doi.org/10.1021/acs.energyfuels.9b00160.